Nanoscale Advances

ROYAL SOCIETY OF CHEMISTRY

PAPER

View Article Online
View Journal | View Issue

Cite this: *Nanoscale Adv.*, 2023, **5**, 6078

Graphene oxide nanosheets augment silk fibroin aerogels for enhanced water stability and oil adsorption†

Catherine E. Machnicki,[ab] Eric M. DuBois, ‡[a] Meg Fay,[ab] Snehi Shrestha,[c] Zachary S. S. L. Saleeba,[a] Alex M. Hruska,[a] Zahra Ahmed,[a] Vikas Srivastava, [a] Po-Yen Chen [c] and Ian Y. Wong *[a]

Nanocomposite aerogels exhibit high porosity and large interfacial surface areas, enabling enhanced chemical transport and reactivity. Such mesoporous architectures can be prepared by freeze-casting naturally-derived biopolymers such as silk fibroin, but often form mechanically weak structures that degrade in water, which limits their performance under ambient conditions. Adding 2D material fillers such as graphene oxide (GO) or transition metal carbides (*e.g.* MXene) could potentially reinforce these aerogels *via* stronger intermolecular interactions with the polymeric binder. Here, we show that freeze-casting of GO nanosheets with silk fibroin results in a highly water-stable, mechanically robust aerogel, with considerably enhanced properties relative to silk-only or silk-MXene aerogels. These silk-GO aerogels exhibit high contact angles with water and are highly water stable. Moreover, aerogels can adsorb up 25–35 times their mass in oil, and can be used robustly for selective oil separation from water. This increased stability may occur due to strengthened intermolecular interactions such as hydrogen bonding, despite the random coil and α-helix conformation of silk fibroin, which is typically more soluble in water. Finally, we show these aerogels can be prepared at scale by freeze-casting on a copper mesh. Ultimately, we envision that these multicomponent aerogels could be widely utilized for molecular separations and environmental sensing, as well as for thermal insulation and electrical conductivity.

Received 22nd May 2023
Accepted 5th October 2023

DOI: 10.1039/d3na00350g

rsc.li/nanoscale-advances

Introduction

Mesoporous architectures assembled by freeze-casting of nanomaterials and polymers exhibit extraordinary surface areas for enhanced interfacial transport and reaction.[1] During this ice-templating process, controlled undercooling of a precursor solution results in a solidification front where the particulates are trapped at a moving interface between solid (*e.g.* ice) and liquid (*e.g.* water).[2] Typically, unidirectional temperature gradients drive the advance of finger-like ice growths with particulates accumulating along the periphery, due to the higher solubility of particulates in the liquid phase relative to the solid phase. These "cellular" ice structures are regularly spaced due to the characteristic wavelength of the Mullins–Sekerka instability, governed by the thermodynamic competition between the particulate concentration gradient and the interfacial energy.[3] After the completion of this process, these ice growths can be removed by sublimation, templating large air-filled pores separated by compacted particulate layers. These so-called aerogels can be understood as an air-filled composite material, where the presence of entrapped, hydrophobic air pockets can greatly affect interactions with hydrophilic liquids (*i.e.* Cassie–Baxter state).[4]

Early pioneering work demonstrated freeze-casting using polymers[5] and ceramic particles,[6] and has been subsequently generalized for a wide variety of metal, composite, and carbon-based materials (see reviews in ref. 1 and 7). Naturally-derived biomaterials such as silk fibroin, cellulose, alginate, or starch are promising since they minimize the use of toxic precursors and hazardous solvents derived from petroleum.[8] The mechanical properties of these biomaterials can be improved by augmenting physical entanglement with hydrogen bonding, ionic interactions, or covalent crosslinking.[8] However, these hydrophilic biopolymers are highly vulnerable to degradation by water, which is exacerbated by rapid moisture uptake in mesoporous architectures under ambient conditions.[9] One potential solution is to prepare composite architectures that reinforce biopolymer binders with nanomaterial fillers. For

[a]*School of Engineering, Brown University, 184 Hope St, Box D., Providence, RI 02912, USA. E-mail: ian_wong@brown.edu*

[b]*Department of Chemistry, Brown University, 324 Brook St, Box H., Providence, RI 02912, USA*

[c]*Department of Chemical and Biomolecular Engineering, University of Maryland, 4418 Stadium Dr College Park, MD 20742, USA*

† Electronic supplementary information (ESI) available. See DOI: https://doi.org/10.1039/d3na00350g

‡ Current Address: Department of Biomedical Engineering, Boston University, 44 Cummington Mall, Boston, MA 02215, USA.

example, so-called two-dimensional (2D) material nanosheets (*e.g.* graphene oxide, transition metal carbides) exhibit exceptional physiochemical properties and large surface areas with functional chemical groups.[10]

Silk fibroin protein (extracted from the silkworm *Bombyx mori*) represents a promising water-soluble precursor for aerogels since it is relatively inexpensive, but on its own forms mechanically fragile and water degradable aerogels.[9] Silk fibroin is a block copolymer with hydrophobic blocks that crystallize into β-sheets, alternating with short hydrophilic blocks that function as linkers.[11] These β-sheet crystalline regions interact *via* hydrogen bonding and van der Waals interactions for intersheet stacking, functioning effectively as crosslinkers, while the hydrophilic linker domains provide elasticity.[12] The spun silk polymorph (silk type II) includes extensive β-sheet crystallites, which results in enhanced mechanical strength, thermal resistance and water stability (insoluble in water).[11] In comparison, glandular silk (silk type I) is typically observed in aqueous conditions, consisting of more amorphous random coil and α-helix conformations, with diminished mechanical strength and high water solubility. Nevertheless, methanol treatment of silk type I can promote β-sheet formation for enhanced crosslinking.[13] Silk fibroin has been previously utilized for aerogels through a variety of processing conditions and chemical modifications.[14–19]

Graphene oxide (GO) is a hydrophilic, chemically modified graphene that can be dispersed as atomically thin nanosheets in water.[20] GO consists of a hexagonal carbon structure with regions of sp^2 and sp^3 carbon hybridization, where sp^2 regions have equivalent characteristics of pristine graphene and sp^3 regions include oxygen moieties on the basal plane (epoxides and hydroxyl) and edges (carboxyl and carbonyl). Since GO combines highly functional surface groups with an exceptionally large specific surface area (2400 $m^2\ g^{-1}$), it is highly promising as a nanofiller for composite materials, augmenting mechanical properties and chemical stability *via* increased interactions. Past investigations have used graphene or GO in aerogels, often as a composite with other polymeric binders.[21–39] Intermolecular interactions between silk fibroin and GO are thought to occur through electrostatic interactions and hydrogen bonding which could enable increased aerogel stability.[40]

MXenes are 2D materials based on carbides and nitrides of early transition metals, which can be prepared as nanosheets that are only a few layers thick.[41] The general formula for MXenes is given by $M_{n+1}X_nT_x$, where M is the transition metal site, X represents carbon or nitrogen sites, and T indicates a termination functional group (–F, –O, and –OH). In particular, $Ti_3C_2T_x$ exhibits exceptional mechanical, electrical, and optical properties. However, this MXene exhibits limited stability since the surface can spontaneously oxidize in water and oxygen.[42] Recently, MXene has been prepared as an aerogel, often with other polymeric binders.[43–48] For instance, nanocomposite aerogels have been demonstrated elsewhere using 2D material nanosheet fillers and silk fibroin.[16,49] Nevertheless, these previous demonstrations differ substantially from the present work in their extensive use of covalent crosslinking and surface functionalization.[49] It has been reported that MXene nanosheet surfaces permit electrostatic interactions and hydrogen bonding with silk fibroin, but these may be destabilized by hydrophobic edge sites.[50]

In this article, we show that freeze-casting of silk fibroin with GO nanosheets results in a mesoporous aerogel with increased mechanical properties and water stability relative to silk-only or silk-MXene aerogels. Although silk fibroin and GO are hydrophilic on their own, we find that the composite silk-GO aerogels are hydrophobic with high contact angles with water. As a consequence, these silk-GO aerogels can rapidly adsorb 25–35 times their mass in oil, removing oil from water without aerogel degradation. Raman spectroscopy and FTIR suggest partial reduction of GO by silk fibroin, but also that silk fibroin remains in water-degradable random coil or α-helix conformations, which we corroborated using methanol vapor treatment. We further demonstrate that aerogels can be prepared in larger geometries by freeze-casting off patterned templates. Overall, this GO-silk fibroin composite is promising as a highly porous material architecture that can be used for separation membranes, environmental monitoring, energy storage, and thermal insulation.

Experimental section

Materials

B. mori silkworm cocoons were purchased from Treenway Silks (Lakewood, CO). Graphene oxide (0.4 wt%) was purchased from Graphenea (Cambridge, MA). Ti_3AlC_2 MAX powder was purchased from Laizhou Kai Kai Ceramic Materials Co., Ltd, China. Sodium carbonate (Na_2CO_3, S2127), hydrochloric acid (HCl, H1758), lithium bromide (LiBr, 746479), methanol (320390), and ASTM type II deionized distilled water (6442-88) were purchased from Millipore Sigma. Grapeseed oil, naphthenic oil (3-in-1 oil) and mineral oil were purchased from a local grocery store. DYE-LITE was purchased from Tracer Products. Slide-A-Lyzer 3.5 K MWCO G2 30 mL dialysis cassettes (PI87725) and sodium hydroxide (NaOH, S320) were purchased from ThermoFisher Scientific. Polydimethylsiloxane (PDMS), SYLGARD 184 silicone elastomer kit purchased from Ellsworth Adhesives.

Preparation of silk fibroin

Silk fibroin was prepared by extraction from silkworm (*B. mori*) cocoons based on Kaplan's protocol.[51] 4.24 g of Na_2CO_3 was weighed and added to 2 L of ASTM type II deionized distilled water (DI water). The 0.02 M Na_2CO_3 solution was brought to a boil. Pupae were removed from the cocoons and cocoons were cut into pieces. To the boiling Na_2CO_3 solution, 5 g of the cut cocoons were added and boiled for 20 min. During the boil, the cocoons were mixed well using a metal spatula. After 20 minutes, the silk fibroin mass was cooled and rinsed in a 2 L bath of DI water for 20 minutes. This washing step was repeated three more times. After the last wash, the silk fibroin was removed from the water and allowed to dry completely at room temperature. Further details are included in ESI† and ref. 51.

After drying, the silk fibroin fibers and mats were gently teased apart and cut with scissors to help with dissolution back into a stock solution. Typically, a stock solution of 20% (w/v) silk fibroin was prepared with a total volume of 15 mL. To prepare the stock solution, 3 g of the teased SF was added to 12 mL of 9.3 M LiBr, to bring to a final volume of 15 mL. This mixture was then added to a 60 °C oven. Dissolution of silk fibroin in LiBr solution occurred over 4–5 hours, and resulted in a solubilized silk solution that appeared clear to translucent yellow in color.

The suspension of solubilize silk fibroin in LiBr (15 mL, 20% (w/v)) was then added to a dialysis cassette (3.5 kDa, 30 mL). This solution was dialyzed against DI water over the course of 48 h with a total of six water changes at the following time points: 1, 4, 9, 24 and 32 h. After dialysis, the silk fibroin suspension was then centrifuged for 20 min at 5 °C and 5000 rpm. The supernatant was decanted, and the centrifuge process was repeated once more for to achieve the final product. To determine an accurate concentration of the silk fibroin suspension, three sets of 500 μL of the silk fibroin solution were dried and weighed.

Zeta potential measurement

Diluted samples were prepared, with GO and MXene at a final concentration of 0.5 mg mL^{-1} and silk fibroin at a concentration of 5.0 mg mL^{-1}. The pH of the GO and MXene samples was adjusted using NaOH (1 M) and HCl (1 M). Equal volumes of GO/MXene dispersions and the silk solution were combined, resulting in a mixed dispersion consisting of 10 wt% MXene or GO relative to silk fibroin. The zeta potentials of all samples were then measured by a Nano-ZS90 Zetasizer (Malvern Instruments) with DTS1070 capillary cell.

Preparation and freeze-casting of silk-GO aerogels

The GO used in this work was purchased by Graphenea as a suspension of 0.4 wt% GO was then adjusted to pH 10 using NaOH (1 M) or HCl (1 M), dropwise. After determining the concentration of the silk fibroin suspension, the mixture was diluted with pH 12 adjusted DI water to a concentration of 40 mg mL^{-1}. Then, the diluted SF suspension was adjusted to pH 10 using NaOH (0.5 M), dropwise. Note that NaOH should be added slowly with gentle stirring to prevent silk fibroin from crashing out of solution, and vortexing is not recommended for this step. Next, the GO and any necessary pH 10 adjusted DI water was added to the silk solution and vortexed briefly to minimize bubble formation. The silk fibroin – GO precursor solution was then pipetted into the molds. The molds were then covered and set onto a cold plate that was set on top of dry ice to reach a temperature of −78 °C. The mixture was left to freeze and then lyophilized for 24 hours. The final aerogels were stored in a desiccator until use.

The final concentrations of GO to silk fibroin were calculated by solid components (after lyophilization). The addition of GO was determined by weight percent relative to SF weight which was help constant at 20 mg mL^{-1}. Therefore, for a GO 5% (w/w), a final concentration of 2 mg mL^{-1} of GO was added to 20 mg mL^{-1} of SF for a total of 1 mL for each sample.

The mixture was added to PDMS molds made in house using the following method. Using the Dow SYLGARD 184 Elastomer kit, 80 g of PDMS was made by a two-part liquid precursor in a 10 : 1 mass ratio based on manufacturer directions. The mixture was degassed under vacuum for 30 minutes before and after pouring into the molds. The PDMS was left to cure in a 60 °C oven overnight.

Cylindrical wells were punched into PDMS using a 15 mm wide cork borer in a 6 by 6 grid. The final dimensions of the wells were ∼15 mm × 8 mm to hold approximately 1 mL of solution.

Preparation and freeze-casting of silk-MXene aerogels

MXene nanosheet dispersions were prepared by adding 1.0 g of Ti_3AlC_2 MAX powder (Laizhou Kai Kai Ceramic Materials Co., Ltd, China) into the solution containing 1.0 g of lithium fluoride (LiF, 99%, Sigma-Aldrich) and 20 mL of 6.0 M hydrochloric acid (HCl) followed by 24 hour stirring at 400 rpm. at 35 °C. Afterward, the solid residue was washed with deionized (DI) water until the pH value increased to 7.0. Subsequently, the washed residuals were added to 100 mL of DI water, ultrasonicated for 30 minutes under N_2 protection in an ice bath, and then centrifuged at 3500 rpm for 30 minutes. The supernatant was collected as the final dispersion of $Ti_3C_2T_x$ MXene nanosheets with the concentration of *ca.* 5 mg mL^{-1}. $Ti_3C_2T_x$ MXene nanosheets were then characterized by using a high-resolution transmission electron microscope (HRTEM, JEOL 2100F, University of Maryland NanoCenter).

The MXene dispersion was then adjusted to pH 10 using NaOH (1 M) and HCl (1 M), dropwise. The pH adjusted MXene dispersion and any necessary pH 10 adjusted DI water was added to the pH adjusted silk solution and vortexed briefly to minimize bubble formation. The silk fibroin – MXene precursor solution was then pipetted into the molds. The molds were then covered and set onto a cold plate that was set on top of dry ice to reach a temperature of −78 °C. The mixture was left to freeze and then lyophilized for 24 hours. The final aerogels were stored in a desiccator until use.

Density and porosity characterization

Aerogel specimens were weighed using an analytical balance (Mettler Toledo XS64), and dimensions measured using calipers. The bulk density ρ_b was estimated as the ratio of measured mass M to volume V, $\rho_b = M/V$. Moreover, the porosity Φ was estimated based on a skeletal density $\rho_s = 1.3$, which was approximated from the density of silk fibroin, and neglecting the small contribution from GO or MXene. Then, $\Phi = (\rho_s - \rho_b)/\rho_s$.

Methanol crosslinking

The lyophilized cryogels were exposed to methanol vapor for 48 h in a Petri dish (100 mm × 20 mm) sealed with parafilm. The container held the cryogels and a smaller container of methanol (35 mm × 10 mm, 10 mL).

Scanning electron microscopy

Scanning Electron Microscopy (SEM) was performed using a Thermo Apreo VS SEM (Thermo Fisher Scientific) at Brown

University's Leduc Bioimaging Facility. To prepare the cryogel samples for SEM, the samples were sliced into 5 mm × 5 mm and 2 mm pieces and transferred onto carbon tape (Ted Pella). Samples were then gold sputtered for 3 min at 20 mA using Emitech K550 sputter. Samples were imaged under 5.0 kV accelerating voltage.

Fourier transform infrared spectroscopy with attenuated total reflectance

Fourier Transform Infrared Spectroscopy with Attenuated Total Reflectance (FTIR-ATR) was performed using a Bruker Alpha II Platinum ATR. Each sample was measured with 64 scans at a resolution of 4 cm^{-1}. The scans were acquired over a wavenumber range of 400–4000 cm^{-1}.

Thermogravimetric analysis

Thermogravimetric analysis (TGA) was carried out on a Shimadzu TGA-50 Series system, with the heating profile starting at 5 °C min^{-1} to 225 °C and then 10 °C min^{-1} up to 800 °C. All of the TGA measurements were carried out under a N_2 flow rate of 60 mL min^{-1}, and the sample masses were controlled to be ~20 mg. The first derivative (DTG) curves were analyzed using OriginPro software.

Raman spectroscopy

Raman spectroscopy was performed using a Witec Alpha 300 Confocal Raman Microscope with a 532 nm laser. The spectra were collected over a wavenumber range of 500–3000 cm^{-1} with an integration time of 10 seconds for 25 accumulations using a 100X objective lens. Spectral manipulation and analysis were performed using the Witec software.

Mechanical characterization

Uniaxial compression testing was performed using an Univert Uniaxial Mechanical Testing system (CellScale) with a 100 N loading cell. The compression rate used was 2 mm min^{-1} and ran until 2 mm of compression was achieved.

Contact angle

Contact angle analysis was performed using Kruss DSA100 Drop Shape Analyzer. Roughly 10 μL droplets of water or oil were manually dispensed onto each sample. The contact angle was collected every 10 seconds up to 2 minutes.

Aerogel water stability

Water immersion tests were conducted by placing aerogels into 20 mL of still DI water for five days. After five days, the cryogels were dried in an oven at 60 °C and weighed using an analytical balance (Mettler Toledo XS64). The difference in the initial and final weight are reported. We did not investigate the role of mechanical agitation, since fracture of the aerogel would complicate handling and characterization.

Aerogel oil absorption

Oil absorption tests were conducted by measuring the weight of the oil added to the aerogels at saturation. Excess oil was dabbed off before measurements. To image oil adsorption by the aerogel, naphthenic oil was labeled with a fluorescent UV dye (DYE-LITE), per manufacturer instructions. A UV-A flashlight was used to illuminate the UV dye-labeled oil.

Image analysis of microstructure

SEM images were exported as tif image files then imported into Fiji. The SEM images were cropped to a 1000 μm × 1000 μm area. For pore analysis a 1000 μm line was drawn across the image and a line profile was taken. The line profile curve was smoothed with a 25 point Savitzky–Golay filter. To pick the peaks, the findpeaks command in MATLAB was used with a minimum find peaks value set to 4000, or to a threshold that most accurately reflected the pore sizes. Directionality of the pores were also performed on the SEM images. The SEM images were cropped to a 1000 μm × 1000 μm area. The directionality analysis was performed from 0 to 180° with Nbins set to 45 and using the Fourier components method.

Statistical analysis

All statistical tests were performed using Prism Graphpad. Each measurement was performed with at least 3 samples, prepared separately but from the same silk, GO, or MXene stock solutions.

Results

Ice templating solutions of 2D materials and silk fibroin into mesoporous architectures

Our strategy to prepare aligned, mesoporous architectures utilized directional freezing of aqueous solutions containing silk fibroin alone or mixed with 2D material nanosheets (GO, MXene) at varying concentrations (Fig. S1†). During freeze-casting, aqueous precursor solutions consisting of dispersed 2D nanosheets (0, 1 or 2 mg mL^{-1}) and uncrosslinked silk (20 mg mL^{-1}) were cooled from below, resulting in a temperature gradient (Fig. 1a(i)). As a consequence, a solidification front formed and advanced upwards, consisting of finger-like ice growths with regular lateral spacing (Fig. 1a(ii)). The particulates cannot readily disperse in the solid (ice) phase relative to a fluid (water) phase, so the particulates are typically rejected away from the ice growths (Fig. 1a(iii)). The rejection of particles from the ice front and, subsequently, the growth of finger-like ice protrusions depend on particulate size, concentration, and interfacial free energies.[2] These particulates are typically compacted into dense aggregates, which are likely enhanced by the flat geometry and high aspect ratio of GO nanosheets. Finally, the ice is sublimated away by lyophilization, leaving a highly porous architecture where the solid walls consist of nanosheets and silk fibroin (Fig. 1a(iv)).

In order for freeze-casting to occur, both silk fibroin and GO needed to remain stably dispersed in aqueous solution. At pH 7, silk fibroin remained somewhat stable, but could gel *via* crystallization of β-sheets *etc.* (Fig. 1b). Similarly, GO at pH 7 remained stably dispersed in aqueous solution due to its high

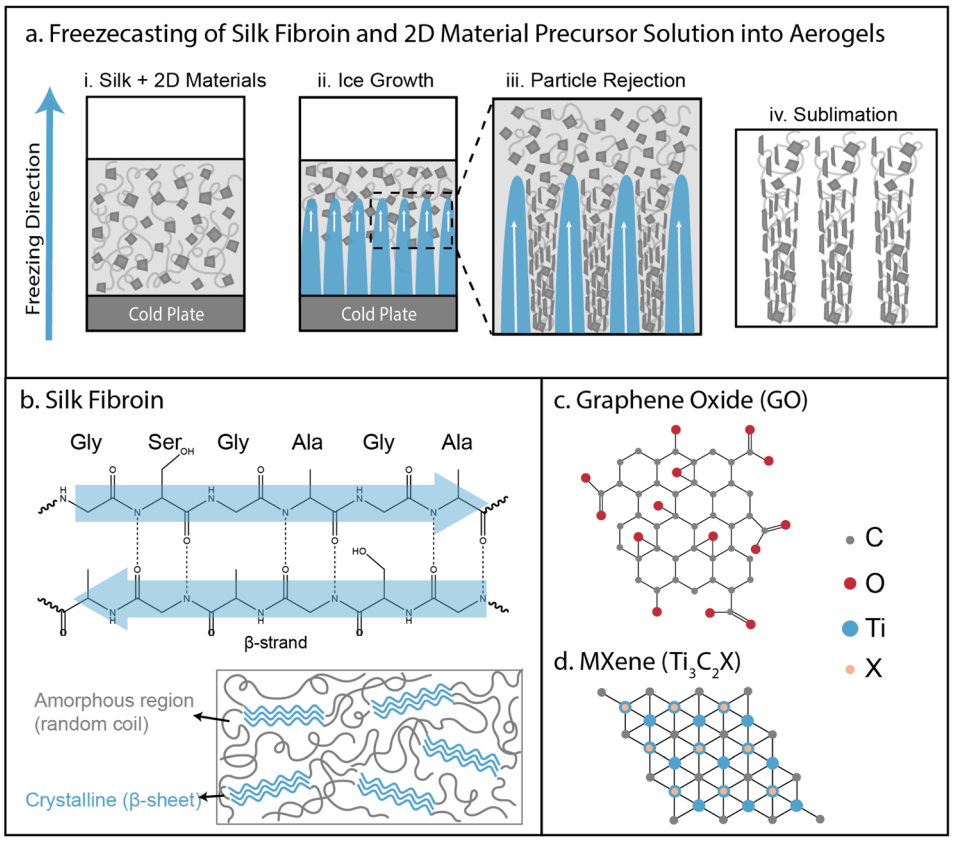

Fig. 1 Strategy for preparing silk-2D material aerogels. (a) Schematic for freeze-casting. Aqueous precursor solutions of dispersed silk fibroin and 2D material nanosheets in a temperature gradient (i), results in the directional growth of finger-like ice structures with periodic spacing, as well as the rejection of dispersed particulates into the liquid phase ((ii) and (iii)). Subsequent sublimation removes ice, templating a mesoporous architecture where lamellar walls consist of compacted nanosheets and silk fibroin (iv). (b) Peptide backbone of silk fibroin consists of Gly, Ser, Ala, which can fold into β-sheets that crystalize, separated by amorphous random coil regions. (c) Chemical structure of graphene oxide includes carbon (C) and oxygen (O) surface groups. (d) Chemical structure of MXene includes titanium (Ti), carbon (C), and terminal functional groups (X, usually fluorene or oxygen).

negative electrostatic surface charge, but weakly interacted with itself *via* hydrogen bonding, π–π stacking, *etc.* (Fig. 1c). Although GO or silk alone were stable in aqueous solution at pH 7, mixing GO and silk resulted in rapid aggregation (Fig. S2a and b†). This was exacerbated at pH 2.5, since lowering pH is known to trigger β-sheet formation (Fig. S2b†). Instead, silk and GO remained stably dispersed at pH 10 (Fig. S2b†), which was likely because most of the silk fibroin residues have a $pK_a < 10$, and would be strongly charged, increasing electrostatic repulsion and limiting aggregation with nanosheets.[11] Moreover, silk and MXene also aggregated at pH 2.5, but remained dispersed above pH 4.5, while MXene alone remained dispersed from pH 2.5–10 (Fig. S2c and d†). These qualitative behaviors were validated using zeta potential measurements, which revealed more negative values for GO and MXene only (from −30 to −40 mV), while silk-GO and silk-MXene remained dispersed but with less negative values (from −20 to −25 mV) at higher pH (Fig. S2e†).

Mechanical stiffness increases with increasing GO concentration in silk fibroin

Scanning electron microscopy (SEM) was performed to compare the porous microstructure of silk-only aerogels relative to composite silk-nanosheet aerogels. For ease of comparison, all aerogels contained 20 mg mL^{-1} silk fibroin, with varying weight percent GO (relative to silk fibroin), which we denote hereafter by 0 wt% (0 mg mL^{-1} GO), 5 wt% (1 mg mL^{-1} GO), and 10 wt% (2 mg mL^{-1} GO). For all three aerogel compositions, the freeze-casting resulted in elongated pores aligned in the direction of freezing (Fig. 2a–c). Notably, silk-only aerogels (0 wt%) exhibited lamellar "walls" with somewhat regular spacing of ≈50 μm, measured laterally (Fig. 2a and d). Silk-GO aerogels (5 and 10 wt%) exhibited comparable wall separations which were typically 40–50 μm, which were not statistically different from silk only (Fig. 2b–d). Characterization of directionality of silk-GO aerogel walls revealed decreased alignment in the freezing direction, so that some pores appeared partially enclosed (Fig. 2e–g). Indeed, silk-GO aerogels often exhibited "bridging" structures between adjacent walls, oriented perpendicular to the freezing direction, which have been observed elsewhere for nanocomposite aerogels with alumnia platelets.[52]

Compression tests were conducted to characterize the mechanical properties of silk-GO aerogels relative to silk-only aerogels. For silk-only aerogels (0 wt% GO), the stress–strain curve was approximately linear out to a strain of $\varepsilon = 8\%$; the

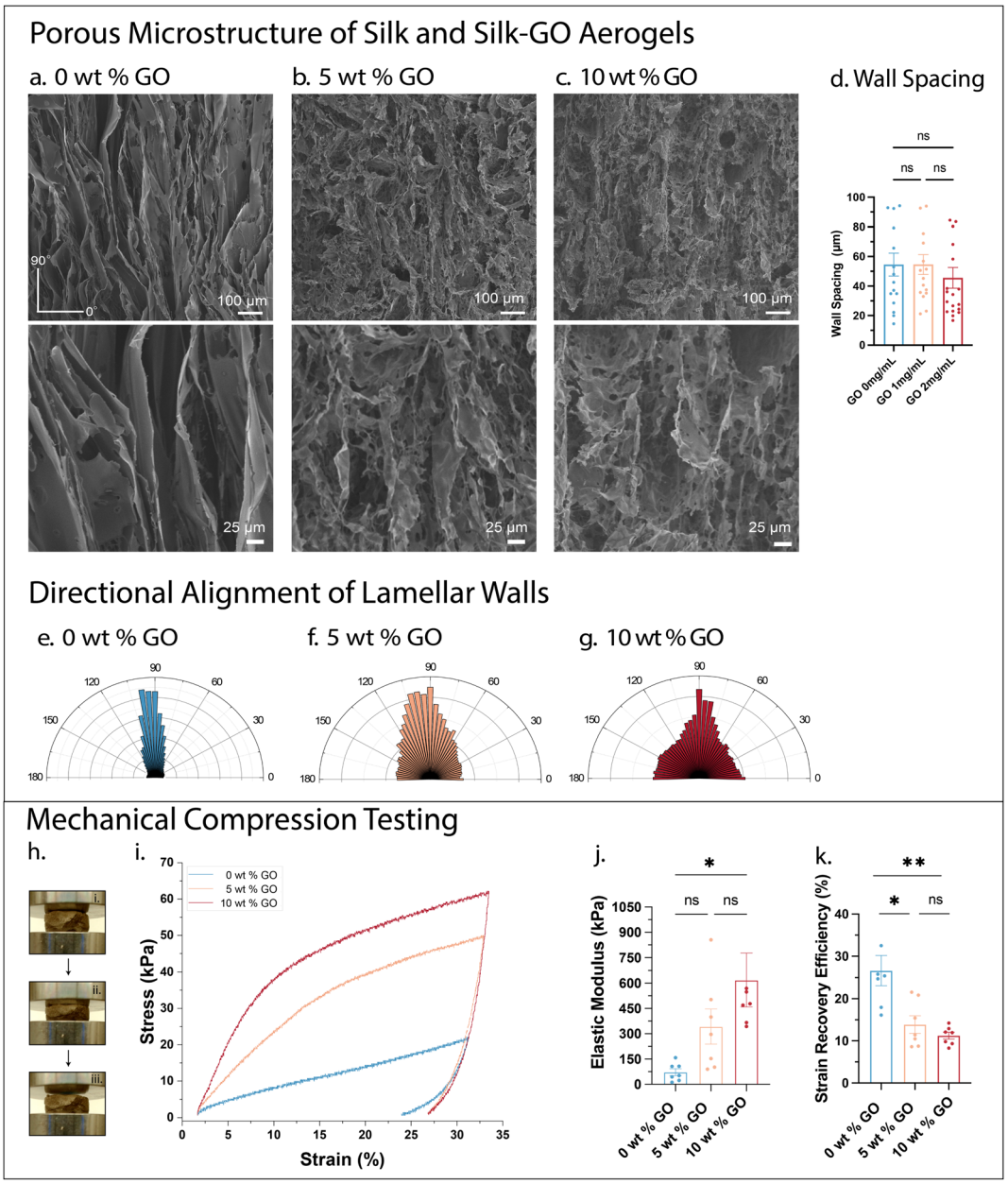

Fig. 2 Microstructure and mechanical characterization of silk-GO aerogels. (a–c) Representative cross-sectional SEM images of silk aerogels (0, 5, 10 wt% GO), at lower magnification (1000 μm × 1000 μm, top) and higher magnification (350 μm × 350 μm, bottom). (d) Comparison of lateral wall separation as a readout of pore size. (e–g) Orientational alignment of lamellar walls relative to freezing direction for silk aerogels (0, 5, 10 wt% GO). (h and i) Representative images of compression testing as well as stress–strain curves for silk-GO aerogels (0, 5, 10 wt% GO). (j and k) Elastic modulus and calculated strain recovery efficiency at 30% strain ($N = 7$ samples tested per condition). Each point denotes a measurement on a different sample, and bar plot shows mean value with error bars denoting standard error of the mean (SEM). One-way ANOVA test for statistics *$p < 0.05$, **$p < 0.01$.

stress–strain response indicates initial elastic response (Fig. 2h and i). In comparison, silk-GO aerogels (5, 10 wt% GO) exhibited a first linear regime with elastic response up to $\varepsilon = 4\%$ strain followed by a less stiff, inelastic response at larger strains, which can be attributed to inelastic buckling of the lamellar walls in porous materials.[53] This linear elastic regime extended out to $\varepsilon = 4\%$ for 5 wt% GO, but only occurred out to $\varepsilon = 2.5\%$ for 10 wt% GO. Silk-only aerogels were relatively weak with low elastic modulus of $E = 72$ kPa (Fig. 2j). In comparison, the addition of GO increased the composite elastic modulus up to $E = 618$ kPa. Further, the strain recovery efficiency as the ratio of elastic and inelastic strain energy was determined to estimate the energy recovered in the aerogel after compression. The silk-only aerogels had a higher strain recovery efficiency than silk-GO aerogels (Fig. 2k). Overall, GO-silk aerogels exhibited higher stiffness and lower energy recovery compared to silk-only aerogels.

Next, composite aerogels of silk fibroin and MXene were prepared with comparable concentrations. These aerogels

exhibited similar aligned architectures with lamellar "wall' spacing averaged at 59 μm for 1 mg mL^{-1} MXene in 20 mg mL^{-1} silk fibroin, and averaged 47 μm for 2 mg mL^{-1} MXene in 20 mg mL^{-1} silk fibroin (Fig. S3a–d†). Similar to silk-GO aerogels, this SEM analysis may not capture open and smaller enclosed pores. The incorporation of MXene nanosheets resulted in an aerogel with sufficient conductivity for SEM imaging without gold sputtering (*via* backscattering detection) (Fig. S3c†). This tunability of aerogel electrical properties using 2D material nanosheets is intriguing and will be characterized more extensively in future work. The silk-MXene aerogels exhibited comparable elastic modulus to silk only aerogels (Fig. S3e and f†). Thus, although silk-GO aerogels exhibited a dramatic increase in elastic modulus relative to silk-only, these trends were not recapitulated in silk-MXene aerogels.

Increased water stability of silk-GO and silk-MXene aerogels

Aerogels with high porosity are often utilized for fluid adsorption and manipulation, since the large interfacial areas regulate the wetting of a liquid onto the solid. Typically, aerogel specimens weighed 19–22 mg for a 1 cm^3 volume, which we use to estimate a density of $\rho \approx 0.02$ g cm^{-3}. We further assume a skeletal density of $\rho_{silk} \approx 1.3$ g cm^{-3},[54] which can be used to estimate a porosity of 98%. We observed minimal shrinkage of the aerogel after drying.

GO and silk are well known to be hydrophilic, which would be expected to promote water spreading and adsorption into the corresponding aerogels. In order to quantify the interactions with water, contact angle measurements were performed on silk aerogels with varying GO concentration (0, 5, and 10 wt% GO) (Fig. 3a–d). Unexpectedly, aerogels with 5 and 10 wt% GO were quite hydrophobic with high contact angles (*e.g.* 110–120°) for 1 μL water droplets (Fig. 3a and b). Further, these contact angles remained relatively constant over 50 s (Fig. 3d), indicating that water was repelled and not adsorbed. In comparison, water droplets deposited on silk-only aerogels (0 wt% GO) were rapidly adsorbed within 50 s (Fig. 3c). The contact angle of a water droplet on these silk-only aerogels decreased rapidly from 110° to 30° within 20 s (Fig. 3d).

These aerogels were then fully immersed in deionized water to compare their stability over much longer durations. Silk aerogels with 10 wt% GO aerogels remained intact indefinitely, whereas silk-only aerogels degraded within 4 min (Fig. 3e). A comparison of dry mass for aerogels prior to immersion and after 5 days in water showed a slight decrease for 5 and 10 wt% GO aerogels and complete dissolution of silk-only aerogels (0 wt% GO) (Fig. 3f). It is likely that swelling of the aerogel after

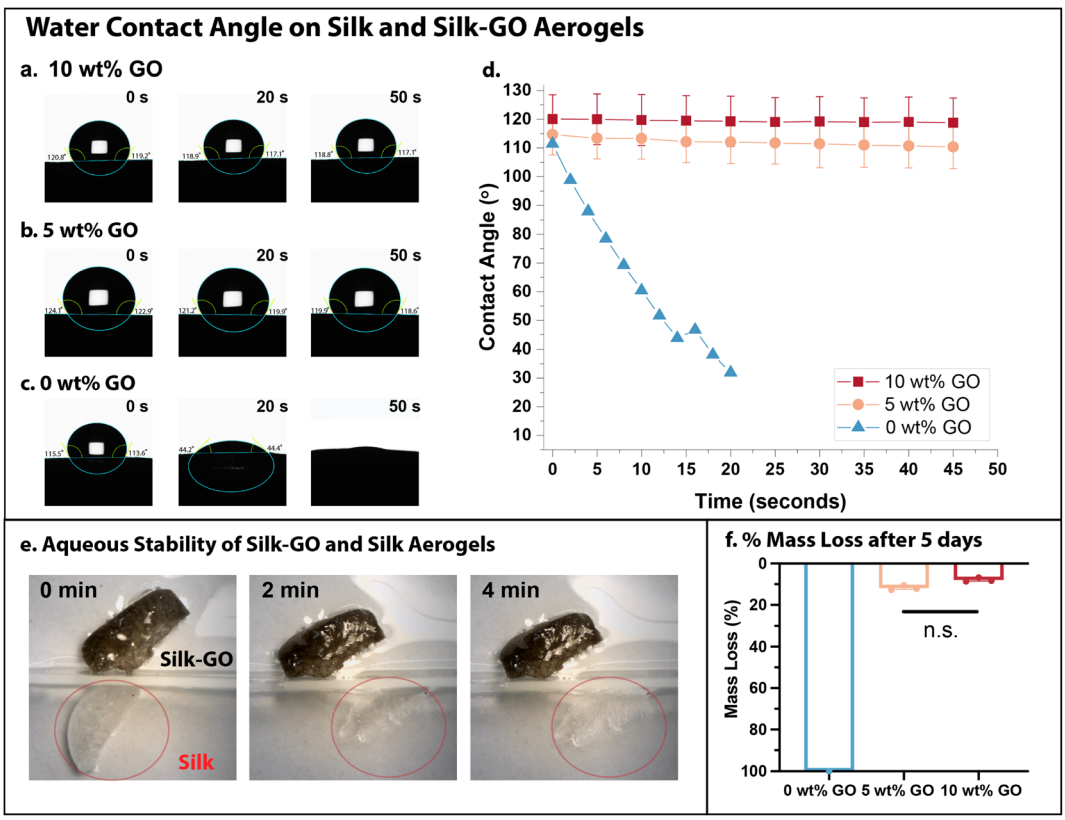

Fig. 3 Interactions of silk-GO aerogels with water. (a–c) Representative contact angle of water on silk aerogels with (10, 5, 0 wt% GO). (d) Average contact angle of water after contacting aerogel surface ($N = 3$ samples). (e) Aqueous stability of silk aerogels (10, 5, 0 wt% GO) after immersion in water for several minutes. (f) Percentage of mass loss for silk aerogels with 5 wt% GO and 10 wt% GO measured after 5 days ($N = 3$ samples). n.s. denotes no significance by student's *t*-test. Note that silk only (0 wt% GO) were fully dissolved after 5 days and cannot be weighed, but has been denoted as 100% mass loss.

water immersion weakened the physical and chemical interactions between silk fibroin and GO, allowing some material to diffuse out. The high water stability of silk-GO aerogels likely contributes to its hydrophobicity, since (hydrophobic) air bubbles can remain trapped at the solid–fluid interface over extended durations. In comparison, the rapid dissolution of silk-only aerogels in water destabilizes air bubbles at the solid–fluid interface that would otherwise contribute towards hydrophobicity.

Similarly, the addition of MXene to silk fibroin aerogels increased water stability relative to silk-only aerogels. For example, a water droplet placed on silk aerogels with 5 or 10 wt% MXene remained stable for at least 5 min (Fig. S4a and b†), whereas water droplets were fully adsorbed by silk-only aerogels (0 wt% MXene) within 1 min. After longer durations of immersion in deionized water, silk aerogels with 5 or 10 wt% MXene exhibited increased mass loss (20–30%) relative to silk aerogels with 5 or 10 wt% GO, but remained intact over 5 days after initial weight loss (Fig. S4c†). Thus, the addition of 2D material nanosheets to silk aerogels increased hydrophobicity and water stability relative to silk only aerogels. Since the enhancement in stiffness, hydrophobicity, and water stability was more pronounced for the additional GO relative to MXene, the following experiments primarily focused on silk-GO aerogels.

High oil absorption of silk-GO aerogels

The hydrophobicity and water stability of silk-GO aerogels was promising for oil absorption applications such as environmental remediation. We considered naphthenic oil, which primarily consists of cyclic alkanes, and mineral oil, which consists of straight alkanes. Grapeseed oil is a vegetable oil with a mixture of fatty acids like linoleic, oleic and palmitic acid. These three oils permit a representative sampling of different physiochemical properties. For example, grapeseed oil has more oxygen containing functional groups than mineral or naphthenic oil. The interaction of grapeseed oil with the silk-only and silk-GO aerogel was quantified with contact angle measurement, revealing rapid absorption of the oil droplet and decreased contact angle within 1 s (Fig. 4a–d).

The oil-absorption capacity of the aerogels was then characterized by adding oil until saturation, then determining the change in mass. Remarkably, aerogels could absorb 25–35 times their mass in naphthenic oil, grapeseed oil, or mineral oil (Fig. 4e and f). For naphthenic oil, silk-GO aerogels exhibited considerably greater oil absorption than silk-only aerogels. The absorption of grapeseed and mineral oils was comparable for silk-only and silk-GO aerogels. As a proof-of-concept, we dispersed 0.5 mL of mineral oil (labeled with a fluorescent UV dye) in 100 mL of water, and showed that a silk-GO aerogel adsorbed the oil within 2 s, without any degradation due to the water (Fig. 4g).

Physicochemical characterization of graphene oxide interactions with silk fibroin

First, Raman spectral analysis was conducted on silk, silk-GO, and GO-only aerogels to probe chemical structure and silk conformation. For GO-only aerogels (4 mg mL^{-1} GO, denoted 100 wt% GO), characteristic peaks occurred at 1348 cm^{-1} (disordered, D band) and 1593 cm^{-1} (E_{2g}, G band) (Fig. 5a). Additionally, two weaker bands were present at 2688 cm^{-1} (2D band overtone) and 2921 cm^{-1} (D + G band overtone) (Fig. 5a, inset). The I_D/I_G intensity ratio (ratio of intensity of the D band to intensity of the G band) is 1.13 by height, indicating disorder from the oxygenated functional groups on GO. In comparison, for silk aerogels with 10 wt% GO, the D and G band peaks shift to 1340 cm^{-1} and 1574 cm^{-1}, respectively. The I_D/I_G intensity ratio decreases to 1.01 by height. Additionally, a sharper peak around 2671 cm^{-1} emerges, which may be attributed to the 2D band overtone. The decrease in I_D/I_G ratio as well as the increase in the 2D band suggests a slight reduction of GO, has been attributed to amino acid reaction (*e.g.* glycine and tyrosine) on the oxygenated functional groups of GO.[55] Finally, for silk-only aerogels (0 wt% GO), the peak at 1103 cm^{-1} and lack of peak at 1083 cm^{-1} was indicative of α-helix conformation, a secondary structure involving alanine (Fig. 5b). Moreover, peaks at 1250 cm^{-1} (amide III) and 1660 cm^{-1} (amide I) correlate to random coil structure (Fig. 5b). The ratio of intensities at 830 and 850 cm^{-1} are associated with the positioning of tyrosine residues. The strong peak at 851 cm^{-1} suggests that the tyrosines are buried in a hydrophobic environment, as seen in silk I.

Further intermolecular interactions between silk fibroin and GO were analyzed using Fourier transform infrared (FTIR) spectroscopy. Silk fibroin has characteristic vibration bands that correlate with amide groups on the peptide backbone. For instance, absorption peaks between 1600 and 1700 cm^{-1} can be assigned to amide I (C=O stretching), 1520–1540 cm^{-1} assigned to amide II (N–H bending), 1517 cm^{-1} for tyrosine side-chains and around 1230 cm^{-1} assigned to amide III (C–N stretching).[56] Moreover, β-sheet absorption peaks typically occurred around 1695 cm^{-1} and 1620 cm^{-1} (amide I), 1520 cm^{-1} (amide II), and 1270 cm^{-1} (amide III), while random coil and α helix conformations occurred around 1640 cm^{-1} (amide I), 1540 cm^{-1}, and 1230 cm^{-1}.[56] Our FTIR measurements of silk-only aerogels (0 wt% GO) as well as silk aerogels with 10 wt% GO showed absorption bands at 1643, cm^{-1}, 1533 cm^{-1}, 1515 cm^{-1} and 1233 cm^{-1}, suggestive of a random coil formation (Fig. 5c). GO-only absorption peaks were measured at 1717 cm^{-1} (C=O), 1623 cm^{-1} (C=C), 1371 cm^{-1} (C–O), 1236 cm^{-1} (C–O–C), and 1065 cm^{-1} (C–O) (Fig. 5d). It should be noted that the absorption peaks associated with GO functional groups are not measurable in the composite spectra, likely due to the 10-fold higher concentration of silk fibroin in these aerogels. Thus, both FTIR and Raman analyses show that silk fibroin primarily occurred as a random coil or α helix conformation rather than β-sheet in these aerogels, even after the addition of GO nanosheets.

Finally, the thermal stability of pulverized aerogel samples was characterized using thermogravimetric analysis (TGA). 10 wt% GO, 10 wt% MXene and 0 wt% GO (silk only) aerogels all exhibited ≈10% mass loss out to 250 °C (Fig. 5e and f). Thereafter, 10 wt% GO aerogels exhibited gradual mass loss down to 20% remaining by 800 °C. In comparison, 10 wt% MXene aerogels exhibited slightly faster mass loss down to 10% remaining by 570 °C, suggesting that the silk fibroin was fully decomposed. Finally, silk-only aerogels showed slightly faster mass loss than 10 wt%

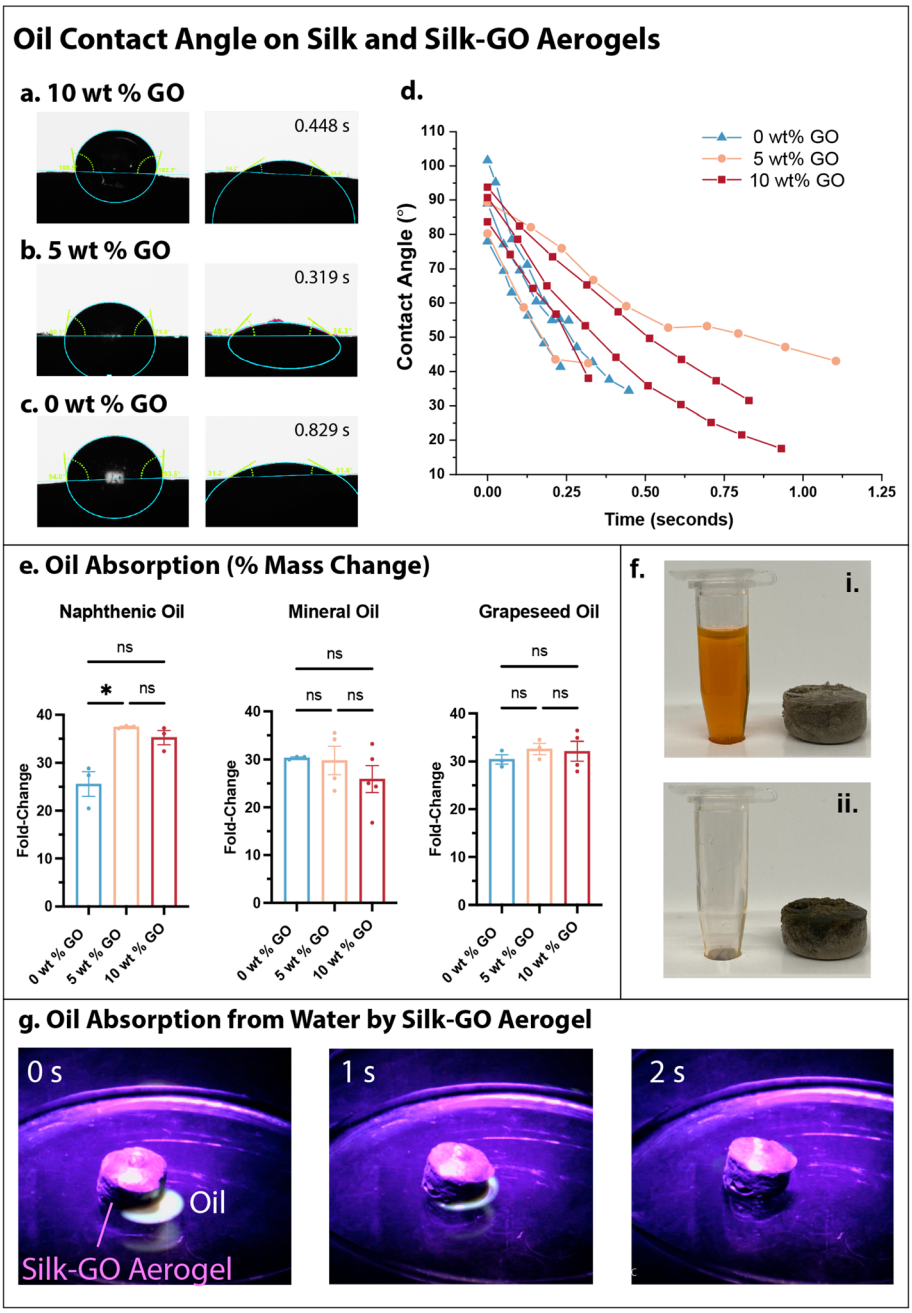

Fig. 4 Interactions of silk-GO aerogels with oil. (a–c) Representative contact angle of grapeseed oil on silk aerogels (10, 5, 0 wt% GO). (d) Average contact angle of grapeseed oil after contacting aerogel surface. (e) Oil adsorbed as fold change in mass for naphthenic oil, grapeseed oil and mineral oil for all conditions. Bar plot shows x as mean values and error bars as standard error of the mean (SEM) ($N = 4$ samples). Two-way ANOVA test, * denotes $p < 0.05$. (f) Representative before and after images of total oil adsorption by silk aerogel with 10 wt% GO. (g) Representative images of oil adsorption from a container of water by a silk aerogel with 10 wt% GO over 2 s. For ease of visualization, oil has been labeled with a phosphorescent dye and illuminated with UV light.

MXene beyond 250 °C, but was slightly more stable past 500 °C. Nevertheless, silk-only aerogels were fully decomposed by 675 °C. Thus, silk-GO aerogels are appreciably more stable than silk-only and silk-MXene aerogels.

Methanol treatment increases water stability of silk fibroin

To further corroborate whether the high water solubility of silk-only aerogels was due to random coil or α-helix conformation, we sought to induce β-sheet crystallite formation after freeze-casting by methanol treatment.[13] FTIR of silk-only aerogels (0 wt% GO) showed a shift in the amide I band to 1621 cm^{-1} with a shoulder peak at 1696 cm^{-1}, as well as weaker shoulder peaks at 1529 cm^{-1} and 1265 cm^{-1}, indicative of β-sheet formation (Fig. 6a). Similar shifts were observed in silk aerogels with 10 wt% GO, also indicative of β-sheet formation after methanol treatment (Fig. 6b). Nevertheless, SEM of the aerogels

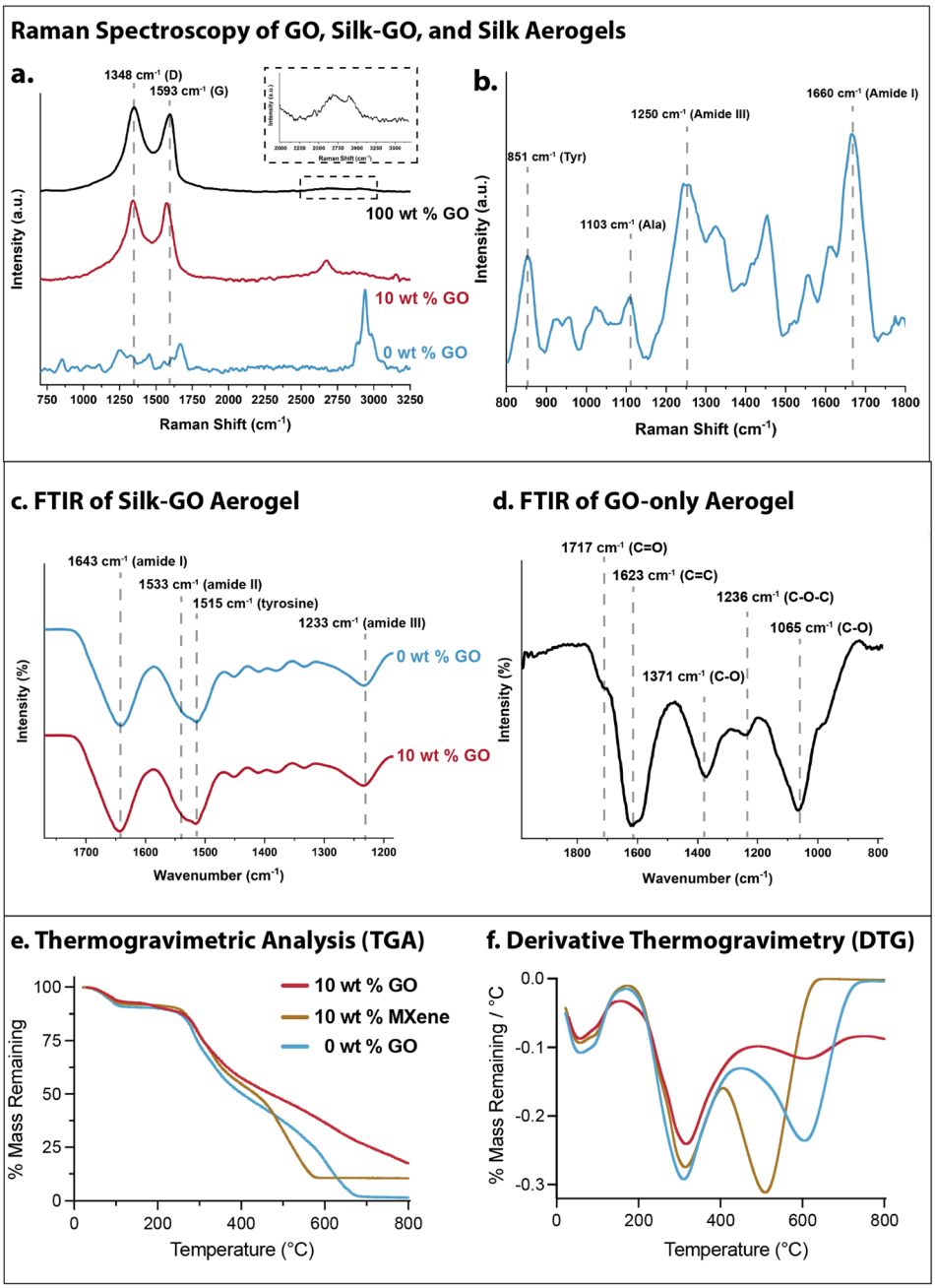

Fig. 5 (a) Raman spectra for 100 wt% GO (4 mg mL^{-1} GO); silk aerogels (10, 0 wt% GO). (b) Raman spectra highlighting 800–1800 cm^{-1} for silk-only aerogels (0 wt% GO). (c) FTIR of silk aerogels (0, 10 wt% GO). (d) FTIR of 100 wt% GO aerogel (4 mg mL^{-1} GO). (e) Thermogravimetric analysis (TGA) and (f) derivative thermogravimetry (DTG) of pulverized silk aerogels (10, 0 wt% GO and 10 wt% MXene).

after methanol treatment revealed qualitatively similar microstructures as pristine aerogels, with pores of comparable spacing across all conditions (Fig. 6c–e). The silk-only methanol treated aerogels (0 wt% GO) had ≈40 μm spacings, not significantly different than pristine silk-only aerogels at ≈50 μm. Silk aerogels with 5 or 10 wt% GO had measured spacings to be ≈50–60 μm, similar to the spacings measured in pristine conditions. Moreover, aerogel mechanical properties after methanol treatment were comparable to pristine aerogels (Fig. 6f). Thus, methanol treatment of aerogels drives β-sheet formation in silk fibroin without appreciably altering microstructure or mechanical properties.

However, water contact angle of methanol treated aerogels was similarly high (110°) and stable for minutes for silk-only and silk-GO aerogels (Fig. S6a–d†). After immersion in DI water, these methanol-treated aerogels exhibited low mass loss (5–8%) (Fig. S6e†), similar to the untreated silk-GO aerogels (Fig. 3f). In addition, methanol-treated silk-only aerogels exhibited about 20-fold naphthenic oil adsorption, which was decreased from the 25-fold oil adsorption for untreated silk-

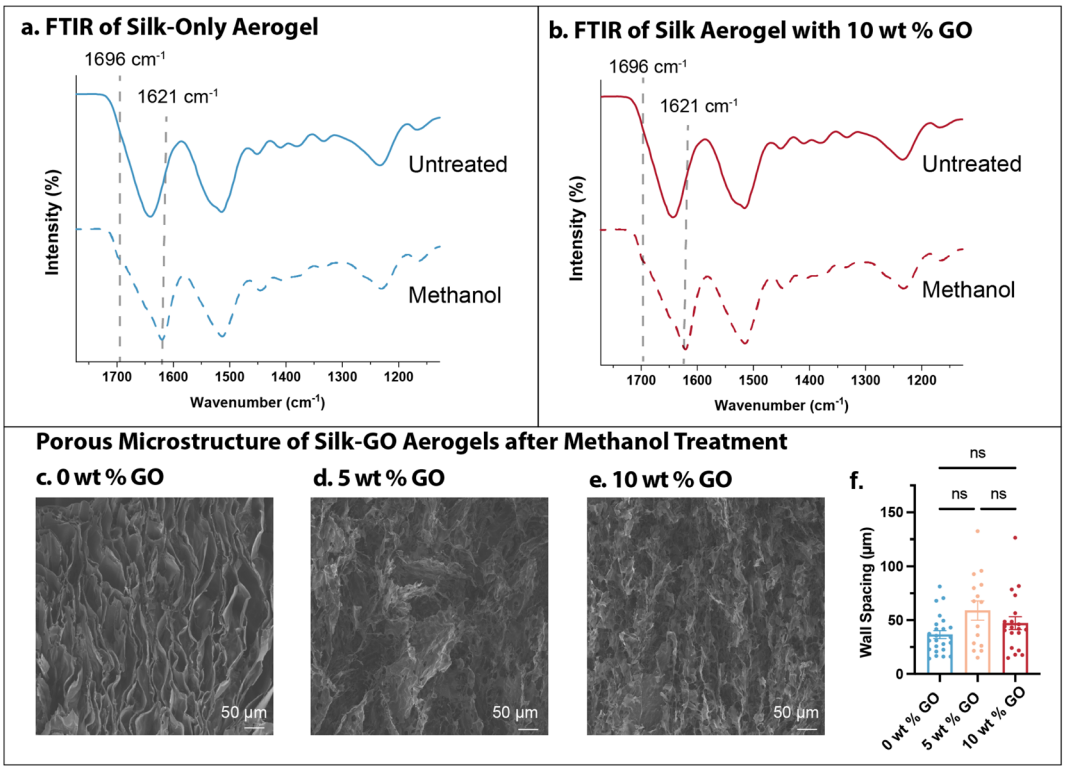

Fig. 6 (a and b) FTIR for amide region in untreated and methanol treated silk aerogels (0, 10 wt% GO). (c–e) Representative SEM images for methanol treated silk aerogels (0, 5, 10 wt% GO). (f) Comparison of lateral wall spacing for silk-GO aerogels. Bar plot shows mean value with error bars denoting standard error of the mean (SEM). One-way ANOVA test for statistics, n.s. denotes no significance.

only aerogels (Fig. 4e and S6f†). Nevertheless, methanol-treated silk-GO aerogels exhibited comparable 30-fold oil adsorption relative to untreated silk-GO aerogels (Fig. 4e and S6f†).

Finally, as a proof-of-concept for much larger specimens, silk-GO aerogels were freeze cast from a copper wire mesh placed on a Petri dish and sandwiched with a PDMS mold with a cylindrical cutout region to expose the copper mesh 25 mm wide (Fig. S7a†). The copper mesh had a wire size of 0.15 mm and opening size of 0.48 mm. After freeze-casting, a monolithic block of 25 mm wide and about 5 mm high was prepared, which replicated the grid-like copper mesh texture into the aerogel (Fig. S7b†). Interestingly, the aerogel surface was relatively smooth, suggestive of a skin-like layer, whereas the grid-like features revealed more exposed silk-GO textured features (Fig. S7c†), comparable in size to the smaller aerogels prepared previously (Fig. S7c†). These hierarchical channel-like surface features could be further utilized for interfacial manipulation of water and oil.

Discussion and conclusion

We demonstrate a facile approach for nanocomposite aerogels that integrates silk fibroin and 2D materials without the use of organic solvents. Freeze-casting of the aqueous precursor solution resulted in a highly anisotropic mesoporous material, where the lamellar walls consist of tightly compacted silk fibroin and 2D material nanosheets. These "cellular" architectures exhibited regular periodic spacing due to the Mullins–Sekerka instability in a unidirectional temperature gradient (Fig. 2a–c).[3] Further control over the pore size and organization could conceivably be achieved using bi-directional temperature gradients, which have been demonstrated using elastomeric wedges[36] as well as cylindrical molds.[38]

Mechanically, the addition of GO nanosheets reinforced the silk fibroin and increased the stiffness under compression (Fig. 2d and e). This also resulted in the earlier onset of a plateau regime in the stress–strain curve, associated with buckling of the lamellar walls. In comparison, the addition of MXene to silk fibroin did not significantly affect the aerogel mechanical properties relative to silk fibroin only, which appear to be dominated by the elasticity of silk (Fig. S3d and e†). These results suggest weaker overall interactions between silk and MXene nanosheets, so there is limited reinforcement of the composite relative to silk and GO. Nevertheless, these MXene aerogels were somewhat conductive when observed using scanning electron microscopy, and could potentially be utilized for strain sensing or electromagnetic interference shielding applications.[57] Since 2D materials are exceptionally strong in tension but not in compression, we anticipate that these effect of these nanofillers on aerogel mechanical properties would be even more pronounced under tension or shear deformations.[58]

We further showed that 2D material nanosheets greatly enhanced the water stability of silk fibroin (Fig. 3), which typically degrade quickly due to their α-helix and random coil

conformation.[11] We prepared our precursor solution of 2D materials and silk fibroin at pH 10, which allowed these components to remain stably dispersed in aqueous solution without crashing out, consistent with zeta potential measurements (Fig. S2e†). Our subsequent characterization with TGA showed that silk-GO aerogels exhibit increased thermal stability relative to silk only. Moreover, Raman spectroscopy showed partial reduction of GO, while FTIR showed that silk fibroin remained in water soluble α-helix or random coil conformation (Fig. 5).[9] We also showed that methanol treatment could induce β-sheet formation, which increased the water stability of silk-only aerogels but did not appreciably affect the mechanics or water stability of silk-GO aerogels (Fig. S6†). The stronger interactions in silk-GO relative to silk may be explained by hydrogen bonding between silk and the hydrophilic GO surface,[40] which is also consistent with our bulk mechanical testing (Fig. 2h–k). In comparison, the presence of hydrophobic edge groups on MXene may partially impede hydrogen bonding with silk fibroin, resulting in weaker adhesion and intermediate water stability relative to silk-GO (Fig. S4†).[50] An intriguing possibility is to further enhance the intermolecular interactions between 2D materials and silk fibroin by postprocessing with ionic crosslinking, which we and others have demonstrated previously with other polyelectrolytes to enhance mechanical properties and self-adhesion.[47,59–62]

We primarily utilized smaller sample volumes for cost-effective use of our reagents when optimizing processing conditions. We envision that precursor solutions of silk fibroin and 2D materials could be prepared in a variety of geometries for subsequent freeze-casting. As a proof of concept, we demonstrated deposition of aerogels on a copper mesh substrate to impart a micron sized grid surface texture. Alternatively, smaller structures could be prepared by nozzle-based extrusion of precursor droplets[63] or 3D printed lattices,[33] followed by freeze-casting. Moreover, large area coatings beyond wafer scale could be prepared by doctor blade processing and tape casting.[64] We note that these different processing techniques should be carefully optimized for precursor solution rheology and temperature gradients, which will affect the porosity and anisotropy of the resulting cellular material. An exciting prospect is to further optimize nanocomposite processing and performance based on the diversity of 2D material nanosheets and protein-based biomaterials.[65]

In conclusion, we show that nanocomposite aerogels comprised of GO nanosheets and silk fibroin exhibit enhanced mechanical properties and water stability relative to silk only and silk-MXene aerogels. A crucial step is to disperse 2D material nanosheets with silk fibroin in aqueous solution at pH 10, which prevents these precursors from crashing out. Subsequently, directional freeze-casting and sublimation results in highly aligned mesoporous architectures where the lamellar walls consist of tightly compacted nanosheets and silk. Further, silk-GO aerogels are highly hydrophobic and resist degradation in water, whereas silk-only aerogels rapidly dissolve under comparable conditions. Indeed, silk-GO aerogels can absorb 25–35 times their dry mass in naphthenic, grapeseed, or mineral oil, and can be used for oil–water separation. This enhancement in bulk properties likely occurs due to strengthened intermolecular interactions between GO nanosheets and silk, such as hydrogen bonding. Finally, we demonstrate the versatility of this technique for patterning nanocomposite aerogels on non-planar and large area substrates. Overall, 2D material – silk aerogels are intriguing for technological applications such as environmental remediation in marine environments, chemical separations, batteries, and electromagnetic interference shielding.

Abbreviations

GO	Graphene oxide
MXene	Transition metal carbide
SEM	Scanning electron microscopy
TGA	Thermogravimetric analysis
FTIR	Fourier transform infrared spectroscopy

Author contributions

C. E. M. and I. Y. W. designed research; C. E. M., E. M. D., M. F., S. S., and Z. S. performed research; A. M. H., Z. A., and V. S. contributed new analytic tools; S. S. and P. Y. C. contributed reagents; C. E. M., V. S., P. Y. C. and I. Y. W. analyzed data; C. E. M. and I. Y. W. wrote the paper with feedback from all authors. All authors reviewed the manuscript.

Conflicts of interest

There are no conflicts to declare.

Acknowledgements

The authors thank Prof. Roberto Zenit for use of the contact angle goniometer, Prof. Anita Shukla for use of the FTIR, and Paul Waltz for assistance during COVID-19. We acknowledge support from Brown University for Start-Up Funds (CEM, IYW), the DiMase Family Internship (EMD), and Karen T. Romer Undergraduate Teaching and Research Award (MF). We also acknowledge the National Institutes of Health R01GM140108 (AMH, IYW) and P20GM109035 (IYW).

References

1 G. Shao, D. A. H. Hanaor, X. Shen and A. Gurlo, Freeze Casting: From Low-Dimensional Building Blocks to Aligned Porous Structures-A Review of Novel Materials, Methods, and Applications, *Adv. Mater.*, 2020, **32**, e1907176.
2 S. Deville, *Freezing Colloids: Observations, Principles, Control, and Use*, Springer, 2017.
3 M. E. Glicksman, *Principles of Solidification: An Introduction to Modern Casting and Crystal Growth Concepts*, Springer, 2010.
4 A. Dhyani, J. Wang, A. K. Halvey, B. Macdonald, G. Mehta and A. Tuteja, Design and applications of surfaces that control the accretion of matter, *Science*, 2021, **373**, eaba5010.

5 H. Zhang, I. Hussain, M. Brust, M. F. Butler, S. P. Rannard and A. I. Cooper, Aligned two- and three-dimensional structures by directional freezing of polymers and nanoparticles, *Nat. Mater.*, 2005, **4**, 787–793.
6 S. Deville, E. Saiz, R. K. Nalla and A. P. Tomsia, Freezing as a path to build complex composites, *Science*, 2006, **311**, 515–518.
7 H. Zhang, *Ice Templating and Freeze-Drying for Porous Materials and Their Applications*, Wiley-VCH, 2018.
8 S. Zhao, W. J. Malfait, N. Guerrero-Alburquerque, M. M. Koebel and G. Nyström, Biopolymer aerogels and foams: chemistry, properties, and applications, *Angew. Chem., Int. Ed.*, 2018, **57**, 7580–7608.
9 J. Ren, Y. Liu, D. L. Kaplan and S. Ling, Interplay of structure and mechanics in silk/carbon nanocomposites, *MRS Bull.*, 2019, **44**, 53–58.
10 C. E. Machnicki, F. Fu, L. Jing, P.-Y. Chen and I. Y. Wong, Mechanochemical engineering of 2D materials for multiscale biointerfaces, *J. Mater. Chem. B*, 2019, **7**, 6293–6309.
11 C. Vepari and D. L. Kaplan, Silk as a Biomaterial, *Prog. Polym. Sci.*, 2007, **32**, 991–1007.
12 A. T. Nguyen, Q. L. Huang, Z. Yang, N. Lin, G. Xu and X. Y. Liu, Crystal networks in silk fibrous materials: from hierarchical structure to ultra performance, *Small*, 2015, **11**, 1039–1054.
13 M. Tsukada, Y. Gotoh, M. Nagura, N. Minoura, N. Kasai and G. Freddi, Structural changes of silk fibroin membranes induced by immersion in methanol aqueous solutions, *J. Polym. Sci., Part B: Polym. Phys.*, 1994, **32**, 961–968.
14 F. Ak, Z. Oztoprak, I. Karakutuk and O. Okay, Macroporous silk fibroin cryogels, *Biomacromolecules*, 2013, **14**, 719–727.
15 R. R. Mallepally, M. A. Marin, V. Surampudi, B. Subia, R. R. Rao, S. C. Kundu and M. A. McHugh, Silk fibroin aerogels: potential scaffolds for tissue engineering applications, *Biomed. Mater.*, 2015, **10**, 035002.
16 S. Wang, H. Ning, N. Hu, K. Huang, S. Weng, X. Wu, L. Wu, J. Liu and Alamusi, Preparation and characterization of graphene oxide/silk fibroin hybrid aerogel for dye and heavy metal adsorption, *Composites, Part B*, 2019, **163**, 716–722.
17 Z. Hu, S. Yan, X. Li, R. You, Q. Zhang and D. L. Kaplan, Natural Silk Nanofibril Aerogels with Distinctive Filtration Capacity and Heat-Retention Performance, *ACS Nano*, 2021, **15**, 8171–8183.
18 X. Xie, Z. Zheng, X. Wang and D. Lee Kaplan, Low-Density Silk Nanofibrous Aerogels: Fabrication and Applications in Air Filtration and Oil/Water Purification, *ACS Nano*, 2021, **15**, 1048–1058.
19 Z. Xu, M. Wu, W. Gao and H. Bai, A sustainable single-component Silk nacre, *Sci. Adv.*, 2022, **8**, eabo0946.
20 D. R. Dreyer, S. Park, C. W. Bielawski and R. S. Ruoff, The chemistry of graphene oxide, *Chem. Soc. Rev.*, 2010, **39**, 228–240.
21 J. L. Vickery, A. J. Patil and S. Mann, fabrication of graphene–polymer nanocomposites with higher-order three-dimensional architectures, *Adv. Mater.*, 2009, **21**, 2180–2184.
22 L. Estevez, A. Kelarakis, Q. Gong, E. H. Da'as and E. P. Giannelis, Multifunctional graphene/platinum/Nafion hybrids via ice templating, *J. Am. Chem. Soc.*, 2011, **133**, 6122–6125.
23 L. Qiu, J. Z. Liu, S. L. Chang, Y. Wu and D. Li, Biomimetic superelastic graphene-based cellular monoliths, *Nat. Commun.*, 2012, **3**, 1–7.
24 Z. Xu, Y. Zhang, P. Li and C. Gao, Strong, conductive, lightweight, neat graphene aerogel fibers with aligned pores, *ACS Nano*, 2012, **6**, 7103–7113.
25 X. Mi, G. Huang, W. Xie, W. Wang, Y. Liu and J. Gao, Preparation of graphene oxide aerogel and its adsorption for Cu^{2+} ions, *Carbon*, 2012, **50**, 4856–4864.
26 X. Xie, Y. Zhou, H. Bi, K. Yin, S. Wan and L. Sun, Large-range control of the microstructures and properties of three-dimensional porous graphene, *Sci. Rep.*, 2013, **3**, 1–6.
27 S. Barg, F. M. Perez, N. Ni, P. do Vale Pereira, R. C. Maher, E. Garcia-Tunon, S. Eslava, S. Agnoli, C. Mattevi and E. Saiz, Mesoscale assembly of chemically modified graphene into complex cellular networks, *Nat. Commun.*, 2014, **5**, 1–10.
28 B. Wicklein, A. Kocjan, G. Salazar-Alvarez, F. Carosio, G. Camino, M. Antonietti and L. Bergström, Thermally insulating and fire-retardant lightweight anisotropic foams based on nanocellulose and graphene oxide, *Nat. Nanotechnol.*, 2015, **10**, 277–283.
29 N. Ni, S. Barg, E. Garcia-Tunon, F. Macul Perez, M. Miranda, C. Lu, C. Mattevi and E. Saiz, Understanding mechanical response of elastomeric graphene networks, *Sci. Rep.*, 2015, **5**, 1–14.
30 H. L. Gao, Y. B. Zhu, L. B. Mao, F. C. Wang, X. S. Luo, Y. Y. Liu, Y. Lu, Z. Pan, J. Ge, W. Shen, Y. R. Zheng, L. Xu, L. J. Wang, W. H. Xu and H. A. Wu, Super-elastic and fatigue resistant carbon material with lamellar multi-arch microstructure, *Nat. Commun.*, 2016, **7**, 12920.
31 Y. Lin, F. Liu, G. Casano, R. Bhavsar, I. A. Kinloch and B. Derby, Pristine graphene aerogels by room-temperature freeze gelation, *Adv. Mater.*, 2016, **28**, 7993–8000.
32 Y. Shao, M. F. El-Kady, C.-W. Lin, G. Zhu, K. L. Marsh, J. Y. Hwang, Q. Zhang, Y. Li, H. Wang and R. B. Kaner, 3D freeze-casting of cellular graphene films for ultrahigh-power-density supercapacitors, *Adv. Mater.*, 2016, **28**, 6719–6726.
33 Q. Zhang, F. Zhang, S. P. Medarametla, H. Li, C. Zhou and D. Lin, 3D Printing of Graphene Aerogels, *Small*, 2016, **12**, 1702–1708.
34 Z. Wang, N. M. Han, Y. Wu, X. Liu, X. Shen, Q. Zheng and J.-K. Kim, Ultrahigh dielectric constant and low loss of highly-aligned graphene aerogel/poly(vinyl alcohol) composites with insulating barriers, *Carbon*, 2017, **123**, 385–394.
35 W. Gao, N. Zhao, W. Yao, Z. Xu, H. Bai and C. Gao, Effect of flake size on the mechanical properties of graphene aerogels prepared by freeze casting, *RSC Adv.*, 2017, **7**, 33600–33605.
36 M. Yang, N. Zhao, Y. Cui, W. Gao, Q. Zhao, C. Gao, H. Bai and T. Xie, Biomimetic Architectured Graphene Aerogel with

Exceptional Strength and Resilience, *ACS Nano*, 2017, **11**, 6817–6824.

37 L. Fan, J.-L. Li, Z. Cai and X. Wang, Creating biomimetic anisotropic architectures with co-aligned nanofibers and macrochannels by manipulating ice crystallization, *ACS Nano*, 2018, **12**, 5780–5790.

38 C. Wang, X. Chen, B. Wang, M. Huang, B. Wang, Y. Jiang and R. S. Ruoff, Freeze-Casting Produces a Graphene Oxide Aerogel with a Radial and Centrosymmetric Structure, *ACS Nano*, 2018, **12**, 5816–5825.

39 Y. Cui, H. Gong, Y. Wang, D. Li and H. Bai, A Thermally Insulating Textile Inspired by Polar Bear Hair, *Adv. Mater.*, 2018, **30**, e1706807.

40 A. M. Grant, H. S. Kim, T. L. Dupnock, K. Hu, Y. G. Yingling and V. V. Tsukruk, Silk Fibroin–Substrate Interactions at Heterogeneous Nanocomposite Interfaces, *Adv. Funct. Mater.*, 2016, **26**, 6380–6392.

41 A. VahidMohammadi, J. Rosen and Y. Gogotsi, The world of two-dimensional carbides and nitrides (MXenes), *Science*, 2021, **372**, eabf1581.

42 X. Zhao, A. Vashisth, J. W. Blivin, Z. Tan, D. E. Holta, V. Kotasthane, S. A. Shah, T. Habib, S. Liu, J. L. Lutkenhaus, *et al.*, pH, Nanosheet Concentration, and Antioxidant Affect the Oxidation of $Ti_3C_2T_x$ and Ti_2CT_x MXene Dispersions, *Adv. Mater. Interfaces*, 2020, **7**, 2000845.

43 X. Zhang, R. Lv, A. Wang, W. Guo, X. Liu and J. Luo, MXene aerogel scaffolds for high-rate lithium metal anodes, *Angew. Chem.*, 2018, **130**, 15248–15253.

44 J. Liu, H.-B. Zhang, X. Xie, R. Yang, Z. Liu, Y. Liu and Z.-Z. Yu, Multifunctional, superelastic, and lightweight MXene/polyimide aerogels, *Small*, 2018, **14**, 1802479.

45 R. Bian, G. He, W. Zhi, S. Xiang, T. Wang and D. Cai, Ultralight MXene-based aerogels with high electromagnetic interference shielding performance, *J. Mater. Chem. C*, 2019, **7**, 474–478.

46 Z. Zeng, C. Wang, G. Siqueira, D. Han, A. Huch, S. Abdolhosseinzadeh, J. Heier, F. Nüesch, C. Zhang and G. Nyström, Nanocellulose-MXene biomimetic aerogels with orientation-tunable electromagnetic interference shielding performance, *Adv. Sci.*, 2020, **7**, 2000979.

47 M. Ding, S. Li, L. Guo, L. Jing, S.-P. Gao, H. Yang, J. M. Little, T. U. Dissanayake, K. Li, J. Yang, *et al.*, Metal Ion-Induced Assembly of MXene Aerogels via Biomimetic Microtextures for Electromagnetic Interference Shielding, Capacitive Deionization, and Microsupercapacitors, *Adv. Energy Mater.*, 2021, **11**, 2101494.

48 D. Jiang, J. Zhang, S. Qin, Z. Wang, K. A. S. Usman, D. Hegh, J. Liu, W. Lei and J. M. Razal, Superelastic $Ti_3C_2T_x$ MXene-based hybrid aerogels for compression-resilient devices, *ACS Nano*, 2021, **15**, 5000–5010.

49 M. Bandar Abadi, R. Weissing, M. Wilhelm, Y. Demidov, J. Auer, S. Ghazanfari, B. Anasori, S. Mathur and H. Maleki, Nacre-mimetic, mechanically flexible, and electrically conductive silk fibroin-MXene composite foams as piezoresistive pressure sensors, *ACS Appl. Mater. Interfaces*, 2021, **13**, 34996–35007.

50 M. C. Krecker, D. Bukharina, C. B. Hatter, Y. Gogotsi and V. V. Tsukruk, Bioencapsulated MXene Flakes for Enhanced Stability and Composite Precursors, *Adv. Funct. Mater.*, 2020, **30**, 2004554.

51 D. N. Rockwood, R. C. Preda, T. Yücel, X. Wang, M. L. Lovett and D. L. Kaplan, Materials fabrication from Bombyx mori silk fibroin, *Nat. Protoc.*, 2011, **6**, 1612–1631.

52 D. Ghosh, M. Banda, H. Kang and N. Dhavale, Platelets-induced stiffening and strengthening of ice-templated highly porous alumina scaffolds, *Scr. Mater.*, 2016, **125**, 29–33.

53 L. J. Gibson and M. F. Ashby, *Cellular Solids: Structure and Properties*, Cambridge University Press, Cambridge, England, 2nd edn, 1999.

54 N. Minoura, M. Tsukada and M. Nagura, Fine structure and oxygen permeability of silk fibroin membrane treated with methanol, *Polymer*, 1990, **31**, 265–269.

55 S. Xu, L. Yong and P. Wu, One-pot, green, rapid synthesis of flowerlike gold nanoparticles/reduced graphene oxide composite with regenerated silk fibroin as efficient oxygen reduction electrocatalysts, *ACS Appl. Mater. Interfaces*, 2013, **5**, 654–662.

56 S.-W. Ha, A. E. Tonelli and S. M. Hudson, Structural Studies of Bombyx mori Silk Fibroin during Regeneration from Solutions and Wet Fiber Spinning, *Biomacromolecules*, 2005, **6**, 1722–1731.

57 Y. Li, X. Tian, S.-P. Gao, L. Jing, K. Li, H. Yang, F. Fu, J. Y. Lee, Y.-X. Guo, J. S. Ho, *et al.*, Reversible Crumpling of 2D Titanium Carbide (MXene) Nanocoatings for Stretchable Electromagnetic Shielding and Wearable Wireless Communication, *Adv. Funct. Mater.*, 2020, **30**, 1907451.

58 D. Akinwande, C. J. Brennan, J. S. Bunch, P. Egberts, J. R. Felts, H. Gao, R. Huang, J.-S. Kim, T. Li, Y. Li, K. M. Liechti, N. Lu, H. S. Park, E. J. Reed, P. Wang, B. I. Yakobson, T. Zhang, Y.-W. Zhang, Y. Zhou and Y. Zhu, A review on mechanics and mechanical properties of 2D materials–Graphene and beyond, *Extreme Mech. Lett.*, 2017, **13**, 42–77.

59 T. M. Valentin, S. E. Leggett, P. Y. Chen, J. K. Sodhi, L. H. Stephens, H. D. McClintock, J. Y. Sim and I. Y. Wong, Stereolithographic printing of ionically-crosslinked alginate hydrogels for degradable biomaterials and microfluidics, *Lab Chip*, 2017, **17**, 3474–3488.

60 S. Ling, Q. Wang, D. Zhang, Y. Zhang, X. Mu, D. L. Kaplan and M. J. Buehler, Integration of Stiff Graphene and Tough Silk for the Design and Fabrication of Versatile Electronic Materials, *Adv. Funct. Mater.*, 2018, **28**, 1705291.

61 T. M. Valentin, A. K. Landauer, L. C. Morales, E. M. DuBois, S. Shukla, M. Liu, L. H. Stephens Valentin, C. Franck, P.-Y. Chen and I. Y. Wong, Alginate-graphene oxide hydrogels with enhanced ionic tunability and chemomechanical stability for light-directed 3D printing, *Carbon*, 2019, **143**, 447–456.

62 T. M. Valentin, E. M. DuBois, C. E. Machnicki, D. Bhaskar, F. R. Cui and I. Y. Wong, 3D printed self-adhesive PEGDA–PAA hydrogels as modular components for soft

actuators and microfluidics, *Polym. Chem.*, 2019, **10**, 2015–2028.

63 J. Yun, C. Tu, D. Q. Lin, L. Xu, Y. Guo, S. Shen, S. Zhang, K. Yao, Y. X. Guan and S. J. Yao, Microchannel liquid-flow focusing and cryo-polymerization preparation of supermacroporous cryogel beads for bioseparation, *J. Chromatogr. A*, 2012, **1247**, 81–88.

64 S. W. Sofie, Fabrication of Functionally Graded and Aligned Porosity in Thin Ceramic Substrates With the Novel Freeze? Tape-Casting Process, *J. Am. Ceram. Soc.*, 2007, **90**, 2024–2031.

65 M. C. Demirel, M. Vural and M. Terrones, Composites of Proteins and 2D Nanomaterials, *Adv. Funct. Mater.*, 2018, **28**, 1704990.